



# **Turbulently driven deflagration-to-detonation transition in near-Chandrasekhar white dwarfs: a thesis in Physics.**

Ugalino, Mark Ivan

<https://repository.lib.umassd.edu/esploro/outputs/graduate/Turbulently-driven-deflagration-to-detonation-transition-in-near-Chandrasekhar/9914424800801301/filesAndLinks?index=0>

---

Ugalino, M. I. (2023). Turbulently driven deflagration-to-detonation transition in near-Chandrasekhar white dwarfs: a thesis in Physics [University of Massachusetts Dartmouth].  
<https://doi.org/10.62791/20301>

---

University of Massachusetts Dartmouth

Department of Physics

**Turbulently driven deflagration-to-detonation transition  
in near-Chandrasekhar white dwarfs**

A Thesis in

Physics

by

Mark Ivan Ugalino

Submitted in Partial Fulfillment of the

Requirements for the Degree of

Master of Science

May 2023

We approve the thesis of Mark Ivan Ugalino

Date of Signature

---

Robert Fisher  
Professor, Department of Physics  
Graduate Program Director, Physics  
Thesis Advisor

---

Sarah Caudill  
Assistant Professor, Department of Physics  
Thesis Committee

---

Collin Capano  
Research Computing Specialist, Department of Center for Scientific Computing and Data  
Science Research  
Thesis Committee

---

Jianyi Jay Wang  
Chairperson, Department of Physics

---

Jean VanderGheynst  
Dean, College of Engineering

---

Tesfay Meressi  
Associate Provost for Graduate Studies

## Abstract

Turbulently driven deflagration-to-detonation transition in near-Chandrasekhar white dwarfs  
by Mark Ivan Ugalino

Type Ia supernova (SNe Ia) events are highly luminous explosions used as standardizable candles which play a key role in measuring the equation of state of dark energy and the cosmological expansion of our universe. Despite their key role in cosmology and astrophysics, a complete understanding of the explosion physics that triggers these thermonuclear explosions remains elusive until now. In this thesis, I present the first application of a novel laboratory-validated turbulently driven deflagration-to-detonation transition (tDDT) mechanism for thermonuclear flames to full-star three-dimensional hydrodynamical simulations of near-Chandrasekhar (near- $M_{\text{Ch}}$ ) mass SNe Ia explosions. I discuss the role of turbulence-flame interactions in near- $M_{\text{Ch}}$  SNe Ia explosions, and the statistical characteristics of turbulently-driven flames in our simulations.

## Acknowledgements

This undertaking would not have been possible without the guidance and support of my adviser, Professor Robert Fisher, and of my friends and colleagues, especially Abdullah Al-Shaffi, Prabodha Mudalige, Vrutant Mehta, Khanak Bhargava, Sudarshan Neopane, Niranjan Roy, Jack Sullivan, Mckenzie Ferrari, and Daniel Kosakowski. I will never forget the short yet fruitful journey I had with you. I also wish to thank my loving partner, Agatha, my mother, Mary Jane, my brother, Mario, and my relatives, Mommy E, Nanay Alou, Ninang Susie, Tito Fred and Jarred. Thank you for helping me grow into a man a younger Mark would look up to.

I acknowledge the support from National Aeronautics and Space Administration (NASA) Astrophysics Theory Program (ATP) award 80NSSC18K1013. I also appreciate the computation time on Extreme Science and Engineering Discovery Environment (XSEDE) supercomputer Stampede 2 (TG-AST100038) and University of Massachusetts Dartmouth Carnie (ONR DURIP grant N00014-18-1-2255) whose resources were used for this thesis.

# Contents

List of Figures	vi
List of Tables	vii
Chapter 1 Introduction	1
Chapter 2 Methodology	8
2.1 Hydrodynamical simulations of near-Chandrasekhar mass white dwarfs . . .	8
2.2 Nucleosynthetic yields . . . . .	11
2.3 Turbulence statistical analysis . . . . .	11
Chapter 3 Results	13
3.1 Hydrodynamical simulations of near-Chandrasekhar mass white dwarfs . . .	13
3.2 Turbulence statistical analysis . . . . .	14
3.3 Nucleosynthetic yields . . . . .	15
Chapter 4 Conclusions and possible extensions	26
References	28

## List of Figures

Figure 1.1:	Schematic diagram of a laminar flame evolving in a turbulent field leading to wrinkling due to shear forces acting on the flame surface. . . .	4
Figure 2.1:	Schematic diagram that describes how cells are self-consistently marked for detonation in the module we developed for FLASH. . . . .	10
Figure 3.1:	Velocity magnitude slice plots (units in cm/s) showing different snapshots of flame evolution for normal density runs . . . . .	17
Figure 3.2:	Velocity magnitude slice plots (units in cm/s) showing different snapshots of flame evolution for high density runs . . . . .	18
Figure 3.3:	The uncompensated and compensated ( $E(k) k^{5/3}$ ) turbulent energy spectra for standard density runs ignited 50 km off-center. . . . .	19
Figure 3.4:	The uncompensated and compensated ( $E(k) k^{5/3}$ ) turbulent energy spectra for standard density runs ignited 100 km off-center. . . . .	20
Figure 3.5:	The uncompensated and compensated ( $E(k) k^{5/3}$ ) turbulent energy spectra for high density runs ignited 50 km off-center. . . . .	21
Figure 3.6:	The uncompensated and compensated ( $E(k) k^{5/3}$ ) turbulent energy spectra for high density runs ignited 100 km off-center. . . . .	22
Figure 3.7:	Overlay slice plots showing density , temperature , and $L/L_{CJ}$ (a and c) at the onset of tDDT driven detonation. . . . .	23
Figure 3.8:	3D scatter plot showing the distribution of nucleosynthetic yields, with colors marked to denote the kind of isotope with highest mass fraction .	24

## List of Tables

Table 3.1: Nucleosynthetic yields (stable and radioactive) in excess of $10^{-6}$ solar masses calculated from the $N = 100$ standard density model . . . . .	25
--	----



## Chapter 1 Introduction

SNe Ia events are highly luminous explosions (peak optical luminosity  $\sim 10^9 L_{\odot}$ ) used as *standardizable candles* which play a key role in measuring the equation of state of dark energy and the Hubble-Lemaître parameter. Recent SNe Ia surveys like Pan-STARRS (Scolnic et al., 2018) and the Dark Energy Survey (DES) (Abbott et al., 2019) have significantly reduced the calibration uncertainties for constraining the dark energy equation of state (EOS) parameter  $w$ . We expect that the calibration will dramatically improve as we obtain larger datasets of SNe Ia through the Vera Rubin Observatory scheduled to operate in 2024 (Mao et al., 2022), and the Nancy Grace Roman Space Telescope that will be launched in 2027 (Foley et al., 2019). Aside from cosmology, these missions will also provide us tools to better understand the observed diversity of SNe Ia and the nature of their progenitors.

It has long been established that SNe Ia events arise as a violent explosion of a carbon-oxygen white dwarf (CO WD) (Bloom et al., 2011). However, there are two primary progenitor scenarios which may lead to such outcome. In the single-degenerate (SD) channel (Whelan & Iben Jr, 1973; Greggio & Renzini, 1983; Khokhlov, 1991; Yamaoka et al., 1992; Khokhlov et al., 1993; Arnett & Livne, 1994a,b; Han & Podsiadlowski, 2004; Gamezo et al., 2004; Ma et al., 2013; Seitenzahl et al., 2013; Brooker et al., 2021), a white dwarf accretes from a non-degenerate companion (Livne et al., 1991; Dilday et al., 2012), and reaches the Chandrasekhar limit ( $M_{\text{Ch}}$ ) leading to thermonuclear runaway. On the other hand, the double-degenerate (DD) channel consists of two white dwarfs orbiting each other that may either merge or collide (Mochkovitch & Livio, 1990; Pakmor et al., 2010; Van Kerkwijk et al., 2010; Pinsonneault & Stanek, 2006; Dan et al., 2011, 2012; Shen, 2015; Papish & Perets, 2016; Shen et al., 2018; Boos et al., 2021; Bauer et al., 2021). Recent observations generally disfavor the single degenerate channel as the primary channel for the majority of normal SNe Ia due to the absence of a signature from the stripped companion (Schaefer &

Pagnotta, 2012; Olling et al., 2015; Tucker et al., 2020), and very tight constraints on the hydrogen mass transfer rate which lead to a thermonuclear explosion (Gilfanov & Bogdán, 2010; Pérez-Torres et al., 2014; Nomoto & Leung, 2018; Sand et al., 2021). Consequently, there is a strong interest in the DD scenario and the double detonation scenario (Fink et al., 2010; Tanikawa et al., 2019; Pakmor et al., 2021; Magee et al., 2021).

An improved understanding of the origin of the observed diversity of SNe Ia could help in identifying samples appropriate for our cosmological measurements (Leibundgut & Sullivan, 2018). In particular, a known astrophysical bias in the measurement of the Hubble constant is the host galaxy of the SNe Ia sample we use for calibration. The tendency of brighter SNe Ia samples is to occur in late-type spiral galaxies, hinting a correlation with the progenitor evolution of these events. This effect is accounted for by including the host type in SNe Ia light curve training sets (Hicken et al., 2009; Kenworthy et al., 2021). Other systematic evolutionary effects are expected on the basis of the fundamental properties of nuclear burning with lesser metallicity at higher redshifts (Timmes et al., 2003).

In the single degenerate scenario, a white dwarf accretes mass from its non-degenerate stellar companion until it reaches conditions for convective core ‘simmering’ and, eventually, carbon ignition. Flame bubbles that form upon ignition buoyantly rise and are driven by the background turbulence due to flame instabilities (e.g. Rayleigh-Taylor) and large-scale convective motion inside the white dwarf. Two primary explosive outcomes could arise from this initial subsonic deflagration: a pure deflagration or a deflagration-to-detonation transition (DDT).

In pure deflagration models, the subsonic flame propagates outward and allows for significant pre-expansion of the white dwarf. Nuclear burning in the outer regions thereby produce intermediate-mass elements (IMEs) at lower densities. The IME element Si in particular is the defining characteristic of the classification of spectra of SNe Ia events. However, the explosion energies released by pure deflagration models do not match the observed amount for

normal SNe Ia events. Instead, pure deflagration events naturally fit many of the observed properties of a fainter subclass called type Iax supernovae.

The deflagration-to-detonation transition (DDT) mechanism was then proposed to reproduce key properties of observed normal SNe Ia. The DDT invokes a delayed detonation following an initial subsonic deflagration. In the DDT framework, the initial subsonic deflagration phase burns core material at high densities, which then produces iron-group elements (IGEs) like Fe, Ni and Co, including the radioactive isotope  $^{56}\text{Ni}$  which powers the early light curve of SNe Ia. The pre-expansion of the white dwarf pushes fuel outward at lower density. At a critical flame density ( $\rho_{\text{DDT}}$ ), the deflagration transitions to a detonation that quickly burns the remaining material, producing both iron group elements (IGEs) and IMEs. The transition density parameter is usually set to a value that produces synthetic observables with properties similar to a normal SNe Ia. *Hence, there was until very recently an uncertainty in the link between the pre-explosion white dwarf and the resulting photometric and spectroscopic properties of the ejecta in DDT simulations.*

Despite decades of theoretical and experimental work on the DDT in both astrophysical and terrestrial settings, the explosion physics that explains how the transition could occur in an unconfined medium was unknown for a long time. The multi-scale nature of SNe Ia simulations makes it computationally difficult to capture the DDT self-consistently. The microphysics that governs this transition occurs on the scale of thermonuclear flames (i.e.  $\sim 10^0$  cm), which is five orders of magnitude smaller than the finest resolution used in full star simulations of near- $M_{\text{Ch}}$  white dwarfs (i.e.  $\sim 10^5$  cm). Therefore, a combination of experiments and direct numerical simulations (DNS) that capture the small-scale burning dynamics were required to capture this transition.

Recent experimental and computational work on terrestrial and astrophysical flames have demonstrated for the first time that there is a mechanism that produces detonations from

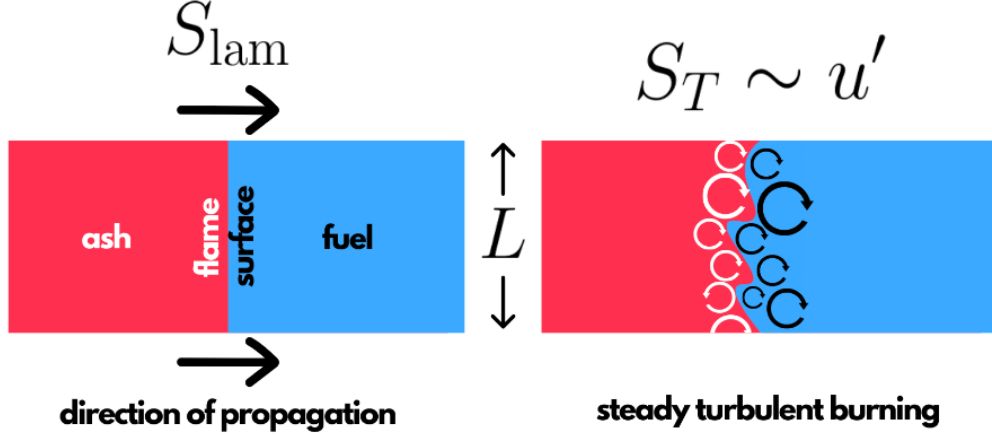


Figure 1.1: Schematic diagram of a laminar flame evolving in a turbulent field leading to wrinkling due to shear forces acting on the flame surface. A flame initially evolves in a laminar fashion as it propagates by heat diffusion through regions with fresh fuel. However, due to the background turbulence, shear forces folds the flame, effectively increasing the local surface area boosting the exothermic reaction rate and the flame speed. It was initially thought by Damkholer that the turbulent flame would equilibriate with the turbulence and reach speeds approximately equal to the root-mean-square turbulent fluctuation velocity  $u'$ . Poludnenko et al. (2019) showed that this is typically not the case, and that the turbulent flame speed could reach values greater than  $u'$  leading to deflagration-to-detonation transition.

strong turbulently-driven deflagration. In combustion theory, when a propagating flame reaches a critical speed, called the Chapman-Jouguet (CJ) speed  $S_{\text{CJ}}$

$$S_T \gtrsim S_{\text{CJ}} = \frac{c_s}{\alpha} \quad (1.1)$$

where  $c_s$  is the sound speed and  $\alpha$  is the fuel-to-ash density ratio  $\rho_f/\rho_a$ , it becomes unstable and proceeds to a pressure runaway. This condition is equivalent to an increase in internal energy  $\varepsilon$  within a local unconfined volume  $L^3$  due to exothermic reactions in the flame within sound-crossing time,

$$\dot{\varepsilon} \gtrsim \frac{\varepsilon}{t_s} \quad (1.2)$$

Thermonuclear deflagration could reach this speed as strong turbulence folds and increases its surface area, boosting the burning reaction rate of the flame (Poludnenko et al., 2011), yielding a turbulent flame speed at a given flame folding scale  $\lambda_f$  given by

$$S_T = I_M S_L \frac{A_T}{L^2} = I_M S_L \frac{L}{\lambda_f} \quad (1.3)$$

where  $I_M$  is the coefficient due to turbulent stretching (usually equal to unity for thermonuclear flames),  $S_L$  is the laminar flame speed, and  $A_T$  is the flame surface area. At the onset of CJ runaway shown in Equation 1.1,

$$\frac{c_s}{\alpha} = I_M S_L \frac{L_{CJ}}{\lambda_f} \quad (1.4)$$

which yields a critical volume define by the CJ length  $L_{CJ}$ ,

$$L_{CJ} = \lambda_f \frac{c_s}{\alpha I_M S_L} \quad (1.5)$$

The minimum achievable scale flames are maximally folded into is the laminar flame thickness  $\delta_L$  which gives rise to a minimum CJ length,

$$L_{CJ} = \delta_L \frac{c_s}{\alpha I_M S_L} \quad (1.6)$$

We can relate this lengthscale criterion to the root-mean-square turbulent fluctuation  $u'$  by assuming that the flame is propagating in homogeneous, isotropic Kolmogorov turbulence. The self-similar statistical characteristics of Kolmogorov turbulence gives a scaling that relates the turbulence strength  $u_\lambda$  at flame folding scale  $\lambda_f$  and  $u_{CJ}$  at critical CJ length scale  $L_{CJ}$ ,

$$\frac{u_{CJ}}{u_\lambda} = \left( \frac{L_{CJ}}{\lambda_f} \right)^{1/3} \quad (1.7)$$

Substituting Equation 1.5 and estimating the turbulent intensity at flame folding scale  $\lambda$ ,  $u_\lambda = \alpha I_M S_L$ , we obtain an expression for the critical turbulent intensity

$$u_{\text{CJ}} = u_\lambda \left( \frac{L_{\text{CJ}}}{\lambda_f} \right)^{1/3} = \alpha I_M S_L \left( \frac{c_s}{\alpha I_M S_L} \right)^{1/3} = c_s^{1/3} (\alpha I_M S_L)^{2/3} \quad (1.8)$$

Notice that this expression for the critical turbulence strength only depends on the properties of the flame. Hence, one can use the Kolmogorov scaling relation above to obtain the critical lengthscale  $L_{\text{CJ}}$  in terms of the turbulence strength  $u_L$  at some arbitrary scale  $L$ ,

$$L_{\text{CJ}} = L \left( \frac{u_{\text{CJ}}}{u_L} \right)^3 = c_s (\alpha I_M S_L)^2 \frac{L}{u_L^3}$$

We can massage this expression to obtain a lengthscale criterion for DDT equivalent to Equation 1.1,

$$\frac{L}{L_{\text{CJ}}} = \frac{u_L^3}{c_s (\alpha I_M S_L)^2} \geq 1 \quad (1.9)$$

Since this mechanism relies only on the interaction of the flame and its background turbulence, detonations arise self-consistently without any need for additional input parameters. This turbulently-driven deflagration-to-detonation (tDDT) mechanism has been well-verified in experimental setups of chemical flames and direct numerical local simulations of thermonuclear flames on the cm scale with conditions similar to white dwarf interiors (Poludnenko et al., 2019).

The onset of a tDDT depends only on the local properties of turbulence inside the white dwarf which may vary according to the initial thermodynamic and ignition conditions of the progenitor (Zingale et al., 2009). Hence, the success of a DDT in the SD scenario can now be directly linked to the properties of the progenitor like central density and metallicity. To fully understand how tDDT-type explosions can contribute to a diverse set of SNe Ia events, we have incorporated the tDDT mechanism as a subgrid-scale (SGS) model in our full-star

three-dimensional simulations of near- $M_{\text{Ch}}$  white dwarfs. In this thesis, we discuss our initial suite of 3D full-star models with varying ignition parameters show that a tDDT-initiated delayed detonation could arise from the transition of an initially Rayleigh-Taylor driven turbulent flame to Kolmogorov turbulence in near- $M_{\text{Ch}}$  white dwarfs (Ugalino et al *in prep*), previously observed in 3D deflagration models by Zingale et al (Zingale et al., 2005). These hydrodynamical explosion models will also be used to obtain detailed nucleosynthetic yields, as well as synthetic light curves and spectra. This thesis is organized as follows. We discuss the methodology that we follow for our hydrodynamic simulations, turbulence analysis, and nucleosynthetic calculations in Chapter 2. We present our full star 3D hydrodynamical simulations and nucleosynthetic yields for select models and our turbulence analysis results in Chapter 3. We end our discussion with key takeaways and present some future work in Chapter 4.

## Chapter 2 Methodology

In this work, we aim to apply *for the first time* a laboratory validated deflagration-to-detonation transition mechanism to full star 3D simulations of near-Chandrasekhar white dwarfs. An important assumption in the model we discussed in the previous chapter is the turbulence statistics of the flame. To determine how the initial conditions of the white dwarf model affect the evolution of the turbulence that drives the flame, we considered four near-Chandrasekhar mass white dwarf models with 2 different central densities (i.e.  $2.2 \times 10^9 \text{ g/cm}^3$  and  $6.0 \times 10^9 \text{ g/cm}^3$ ), and 2 different initial ignition hotspot offsets (i.e. 50 and 100 kilometers). Assuming that the turbulence in the flame is Kolmogorov from  $t = 0$  s, we investigated the local detonation onset conditions according to the tDDT model, and the nucleosynthetic yields produced by single-hotspot ( $N_{\text{bubble}} = 1$ ) and multiple-hotspot ( $N_{\text{bubble}} = 100$ ) near-Chandrasekhar mass white dwarf models with central density  $\rho_c = 2.2 \times 10^9 \text{ g/cm}^3$ .

### 2.1 Hydrodynamical simulations of near-Chandrasekhar mass white dwarfs

We perform 3D full-star simulations using the massively-parallel multi-physics hydrodynamical solver FLASH (Fryxell et al., 2010; Dubey et al., 2009; Dubey et al., 2014). FLASH employs an adaptive mesh refinement strategy to resolve features of the rising ignition hotspot in the stellar interior, capturing Rayleigh-Taylor and Kelvin-Helmholtz instabilities that drives flame propagation at early times. All of our models are resolved up to a maximum 4-kilometer resolution, while the minimum resolution in the fluff region is at 2048 kilometers. The temperature and density were set to  $\rho_{\text{fluff}} = 10^{-3} \text{ g/cm}^3$  and  $T_{\text{fluff}} = 3 \times 10^7 \text{ K}$  in the fluff region around the white dwarf. The refinement and derefinement criteria were based on dimensionless density and flame progress scalar  $\phi$  gradients, where  $\phi$  ranges from 0 (fuel) to 1 (ash). The domain that we use for our simulations extends from  $-6.5536 \times 10^4$



km to  $6.5536 \times 10^4$  km in  $x$ ,  $y$  and  $z$  directions. We selected a domain size approximately 30 times larger than our initial white dwarf model to capture the dynamics of the supernova ejecta a few seconds post-detonation. We use  $10^5$  passive Lagrangian tracer particles for each run to obtain the detailed nucleosynthetic yields for which we need to store the temperature and density histories per simulation timestep. FLASH also use an advection-diffusion-reaction equation to track the evolution of the subsonic flame and its transition to detonation (Townesley et al., 2007, 2009).

To self-consistently detonate our models, we developed a module in FLASH that monitors the local conditions in the flame, specifically the  $L/L_{\text{CJ}}$  criterion. This was done by using both the existing **Burn** and **Flame** modules. A flowchart showing how this is implemented in the code we developed is shown in Figure 2.1. Other than the local properties for the flame, like its laminar flame speed, density, and the local sound speed, we also measure for the turbulence strength which is done online using a calibrated operator called  $\text{OP}_2$  (Colin et al., 2000) defined as,

$$u' = \text{OP}_2(\vec{u}) = c_2^h(\Delta)^3 \nabla^2 (\nabla \times \vec{u}) \quad (2.1)$$

where  $c_2^h$  is a calibrated constant which depends on the stencil used with  $h$  either equal to 1 or 2, and  $\Delta$  is the grid spacing. This operator filters out dilatational contributions to the turbulent fluctuations and was developed by Jackson et al. (2010) for FLASH. They defined the first and second order derivatives as a fourth-order finite central difference defined as,

$$\begin{aligned} \frac{\partial f}{\partial x} &= \frac{f_{i-2h} - 8f_{i-h} + 8f_{i+h} - f_{i+2h}}{12h\Delta} \\ \frac{\partial^2 f}{\partial x^2} &= \frac{-f_{i-2h} + 16f_{i-h} - 30f_i + 16f_{i+h} - f_{i+2h}}{12h^2\Delta^2} \end{aligned}$$

We consider the stencil of the  $\text{OP}_2$  operator  $\Delta_{\text{stencil}} = 4h\Delta$  as the scale  $L$  at which we measure  $u'$ .

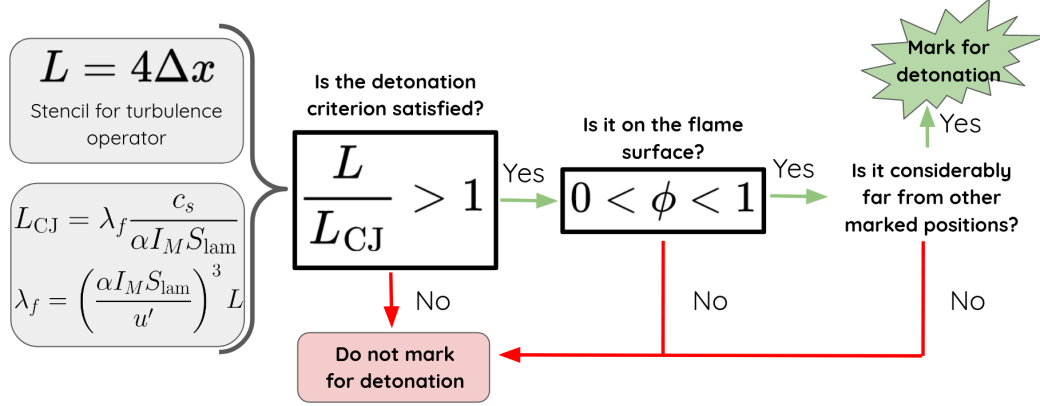


Figure 2.1: Schematic diagram that describes how cells are self-consistently marked for detonation in the module we developed for FLASH. We defined a new grid variable that stores the value of  $L/L_{CJ}$  as defined in a previous chapter. The value of this grid variable is monitored every time step, and checked whether it is equal to or greater than 1. If the cell satisfies this condition, we check if the cell is located in the flame surface using the flame progress variable  $\phi$  that is bounded between 0 (located in the fuel) and 1 (located in the ash). We also make sure that points marked for detonation are not close to other marked points before a detonation is triggered.

## 2.2 Nucleosynthetic yields

Once our hydrodynamical tDDT runs reach nuclear freeze-out, we extracted the temperature and density histories stored by each passive tracer particle and produced a trajectory file per particle. These trajectories were used as input to the nuclear network code Torch (Timmes, 1999b), which uses a general nuclear network coupled with thermodynamics to solve for both stable and radioactive nucleosynthetic yields. For the yields calculated for this thesis, we use a 489-isotope network which is essential to accurately produce synthetic spectra for our models.

## 2.3 Turbulence statistical analysis

In 3D, the turbulent kinetic energy cascades from large to small eddies, each with different length  $L$ . Hence, it is convenient to analyze the background turbulence in Fourier space where we can calculate the power contribution at each scale represented by wavenumber  $\vec{k}$ . We performed a discrete 3D Fourier analysis of the velocity fields in  $x$ ,  $y$ , and  $z$  directions, and calculated the total power given by,

$$E(\vec{k}) = \frac{1}{2} \sum_i^{N^3} (u^* u + v^* v + w^* w)_i \quad (2.2)$$

where  $u$ ,  $v$ , and  $w$  are Fourier transforms of the  $v_x$ ,  $v_y$  and  $v_z$  velocity fields, which is summed over all cells in the  $N^3$  array. We computed this 3D power by first extracting a 1600 kilometer box region in our FLASH dataset, effectively mapping the dataset into a uniform grid at the finest resolution of the simulation using the Python visualization and analysis package `yt`. This box is centered about the average mass-weighted flame progress scalar along the direction of propagation of the flame. We chose  $L = 1600$  km because it would most likely contain the whole flame bubble throughout its whole evolution up until it breaks out of the white dwarf surface. The 3D fourier transform of each velocity box were obtained using the `numpy.fft.fftn` package. To check if the power that we obtain is correct, we invoked the

discrete version of Parseval's theorem which ensures that the power in real space defined as,

$$E(\vec{x}) = \frac{1}{2} \sum_i^{N^3} (v_x^2 + v_y^2 + v_z^2)_i \quad (2.3)$$

would be equivalent to the Fourier power defined in Equation 2.2 through the following relation,

$$\sum_{x,y,z} |f(x, y, z)|^2 = \frac{1}{N^3} \sum_{k_x, k_y, k_z} |F(k_x, k_y, k_z)|^2 \quad (2.4)$$

After calculating the 3D power, we radially binned contributions due to each wavenumber  $k + dk$  and summed these contributions to generate a 1D spectral kinetic energy density plot. To capture the deviation of our turbulence energy spectra from Kolmogorov scaling, we also calculated compensated power spectra  $E(k)k^{5/3}$ .

## Chapter 3 Results

In this chapter, we discuss the results of our simulations and post-processing analysis using the same outline in the previous chapter. We present the hydrodynamical simulations, noting the similarities/differences in structure of the flame bubble for different models. We discuss the turbulent energy spectra we calculated for our models and their implication for the tDDT initiation in our simulations. Lastly, we present the nucleosynthetic yields from tDDT initiated detonation models assuming that the flame is in Kolmogorov turbulence from the start of the simulation.

### 3.1 Hydrodynamical simulations of near-Chandrasekhar mass white dwarfs

As discussed in the previous chapter, we considered four single bubble models with varying central densities and ignition hotspot offsets. These models were not triggered for detonation, but were monitored from ignition up until bubble breakout. Slice plots of velocity magnitudes at specific timesteps are shown in Figure 3.1 for standard density runs, and in Figure 3.2 for high density runs. A noticeable difference between standard and high density runs is the geometry of the flame. The initially spherical flame bubble in standard density runs developed a mushroom-like plume, whereas this plume is split into two branches for high density runs. We also observe that the flame bubble reaches the surface faster in 100 km offset runs, which is expected since the bubble’s evolution at higher offsets is immediately driven by buoyancy (Fisher & Jumper, 2015). At lower offsets, the flame bubble burns through the center before buoyantly rising to the surface. We note that for the high density runs, the simulation resolution derefines at 0.5 second from 4 km to 8 km, contrary to the standard density runs, due to criteria based on density and flame progress scalar gradients. Hence, slice plots for high density runs display a  $3200^3$  box. We use the velocity component

fields from our FLASH runs to generate 1D turbulent kinetic energy spectra which will be discussed in the next section.

### 3.2 Turbulence statistical analysis

Each model were analyzed using a code we developed that employs 3D Fourier analysis to generate 1D turbulent kinetic energy spectra. To check that our Fourier analysis procedure yields correct results, we invoked Parseval’s theorem for discrete Fourier transform, and found that the results we obtained has a root-mean-square error equal to machine precision ( $\sim 10^{15} - 10^{16}$ ). To verify if the radial binning procedure from 3D Fourier space to 1D, we also compared the volume-integrated power in 3D and 1D space. We found good agreement between the spectral powers in 3D and 1D space. Shown in Figures 3.3, 3.4, 3.5, and 3.6 are uncompensated ( $E(k)$ ) and compensated ( $E(k)k^{5/3}$ ) spectra for four models we have considered.

In Figure 3.3, we can see how the spectra evolves over time from 0.1 – 0.8 second after flame ignition for a 50-km offset standard density model. At early times, the power is dominated by noise in the grid but was later driven by the rising motion of the bubble along the  $z$ -axis. The slope of the spectra are noticeably steeper than the  $-5/3$  scaling denoted by gray dashed lines. However, as the flame rises midway in the stellar interior at around 0.7 second, an inertial range with  $-5/3$  slope began to develop at larger scales which can be observed in the compensated spectra. One can also notice a break in the spectra at later times between 10.5 and 31.5 km which most likely corresponds to a numerical dissipative range with slope of  $-10/3$ .

On the other hand, for the 100 km offset run shown in Figure 3.4, we clearly see that the spectra becomes Kolmogorov at  $t = 0.8$  second. However, we can also observe the break in the spectra between the same range of scales as the 50 km offset, which may imply that these are intrinsic to the numerical method used. Changing the resolution of the simulation to a finer grid spacing, i.e.  $\Delta = 1$  or 2 km, may uncover parts of the physical inertial range

buried within numerical dissipation. This effect is more evident in the high density runs where the finest resolution is at  $\Delta = 8$  km, shown in Figures 3.5 and 3.6. While there is a small range of scales where an inertial range with slope of  $-5/3$  can be observed, this is clearly washed out by numerical dissipation. Hence, running these simulations at higher grid resolution could show more features of the inertial range. These higher resolution runs could better improve our measurements of the power law slope since there is a possibility that a  $-5/3$  scaling can be observed at earlier times.

### 3.3 Nucleosynthetic yields

To test the module we wrote for tDDT implementation in FLASH, we also considered the case where tDDT initiated detonations are enabled from the start of the simulation. Two models were simulated, one with a single hotspot and another with 100 hotspots for flame ignition, a realization first implemented by Seitenzahl et al. (2013) to artificially alter the strengths of the deflagration. tDDT initiated detonations are triggered self-consistently, following the flowchart shown in Figure 2.1, and are monitored through modified versions of the **Flame** and **Burn** modules. The thermodynamic history of each passive tracer particle were stored and processed to produce  $10^5$  trajectory files and were used as input to the nucleosynthesis code **Torch** (Timmes, 1999a).

We found that tDDT detonations were promptly triggered for both  $N = 1$  and  $N = 100$  models at  $t = 0.55$  second and  $t = 0.3$  second respectively. The transition densities local to the cells marked for detonation were at  $\rho_c = 2.62 \times 10^8$  g/cm<sup>3</sup> for  $N = 1$ , and  $\rho_c = 1.76 \times 10^9$  g/cm<sup>3</sup> for  $N = 100$  models, which are generally higher than the transition density adopted in the literature at  $\sim 10^7$  g/cm<sup>3</sup>. The local conditions in the flame bubble for both models are shown in overlay slice plots in Figure 3.7.

For the  $N = 100$  model, the global abundances of nucleosynthetic yields we obtained after nuclear freeze-out are shown in Table 3.1. We see that the Ni-56 yield we obtained is at  $0.882 M_\odot$  which is higher than the literature value for normal luminosity Ia events at  $0.6 M_\odot$

(Byrohl et al., 2019). The radioactive isotope with the second highest abundance is Fe-54. The distribution of nucleosynthetic abundances based on baryonic number  $A$  is shown in Figure 3.8. Particles marked red represent high abundances of iron group elements ( $A > 40$ ,  $A \neq 56$  or  $Z \neq 28$ ). Particles marked white represent high abundances of radioactive isotope Ni-56. Particles marked blue represent intermediate mass elements ( $16 < A \leq 40$ ). We see that the highly neutronized iron peak yields are concentrated at the core of the supernova ejecta, while Ni-56 is in the outer envelope. This implies that the early photometric properties of this supernova event is powered by the radioactive isotope Ni-56. Intermediate mass and unburnt (C, O) yields are sparsely distributed in the outermost regions of the ejecta. To generate synthetic spectra, we have to run this simulation for a longer duration up until the ejecta is homologously expanding.



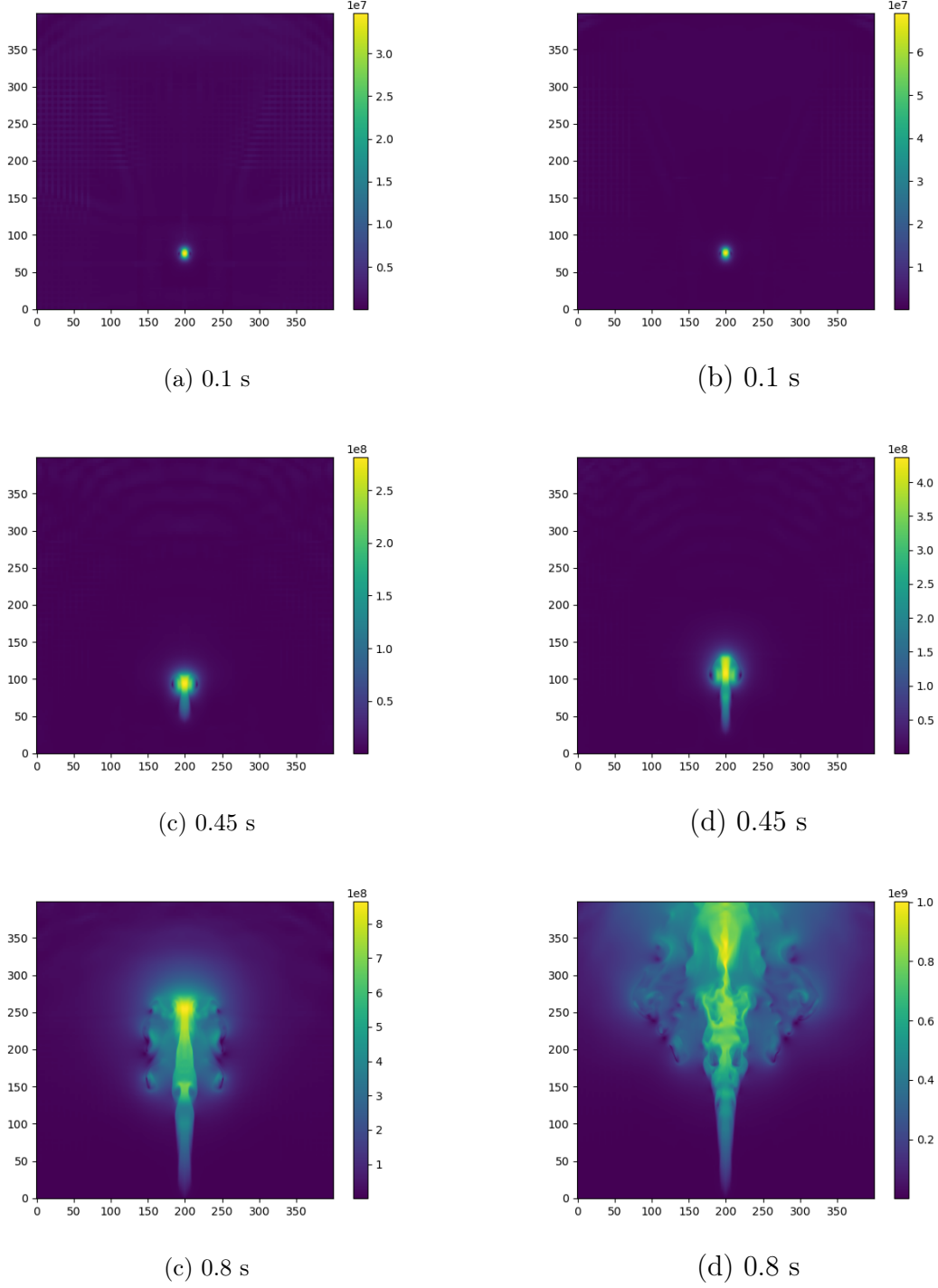


Figure 3.1: Velocity magnitude slice plots (units in cm/s) showing different snapshots of flame evolution for (a-b) an ignition offset of  $5 \times 10^6$  cm, and (c-d)  $1 \times 10^7$  cm, for the standard density ( $\rho_c = 2.2 \times 10^9$  g/cm<sup>3</sup>) near-Chandrasekhar mass model. Each snapshot spans a  $1600^3$  box extracted from our FLASH run.

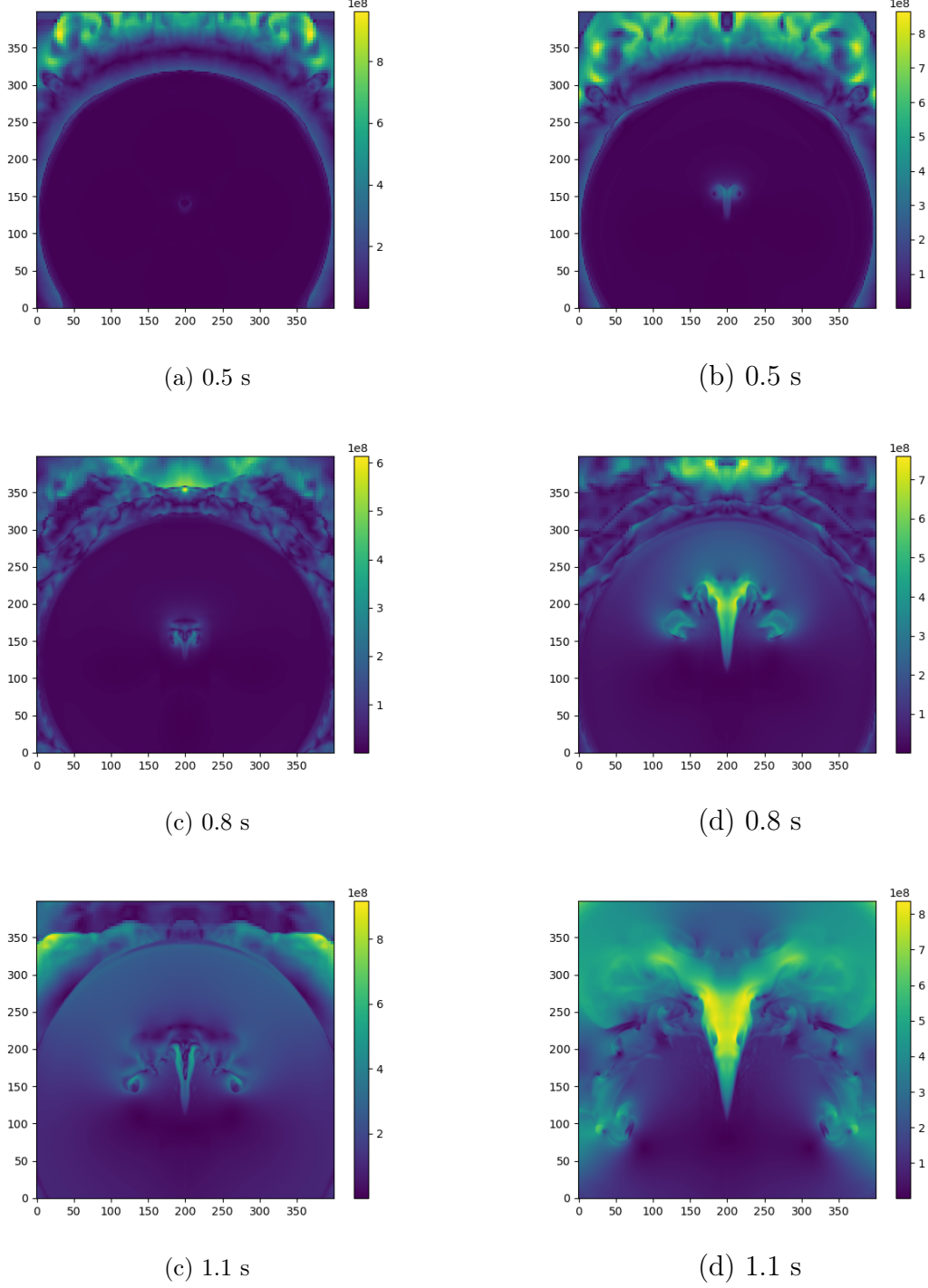


Figure 3.2: Velocity magnitude slice plots (units in cm/s) showing different snapshots of flame evolution for (a-b) an ignition offset of  $5 \times 10^6$  cm, and (c-d)  $1 \times 10^7$  cm, for the high density ( $\rho_c = 6.0 \times 10^9$  g/cm<sup>3</sup>) near-Chandrasekhar mass model. Each snapshot spans a  $3200^3$  box extracted from our FLASH run.

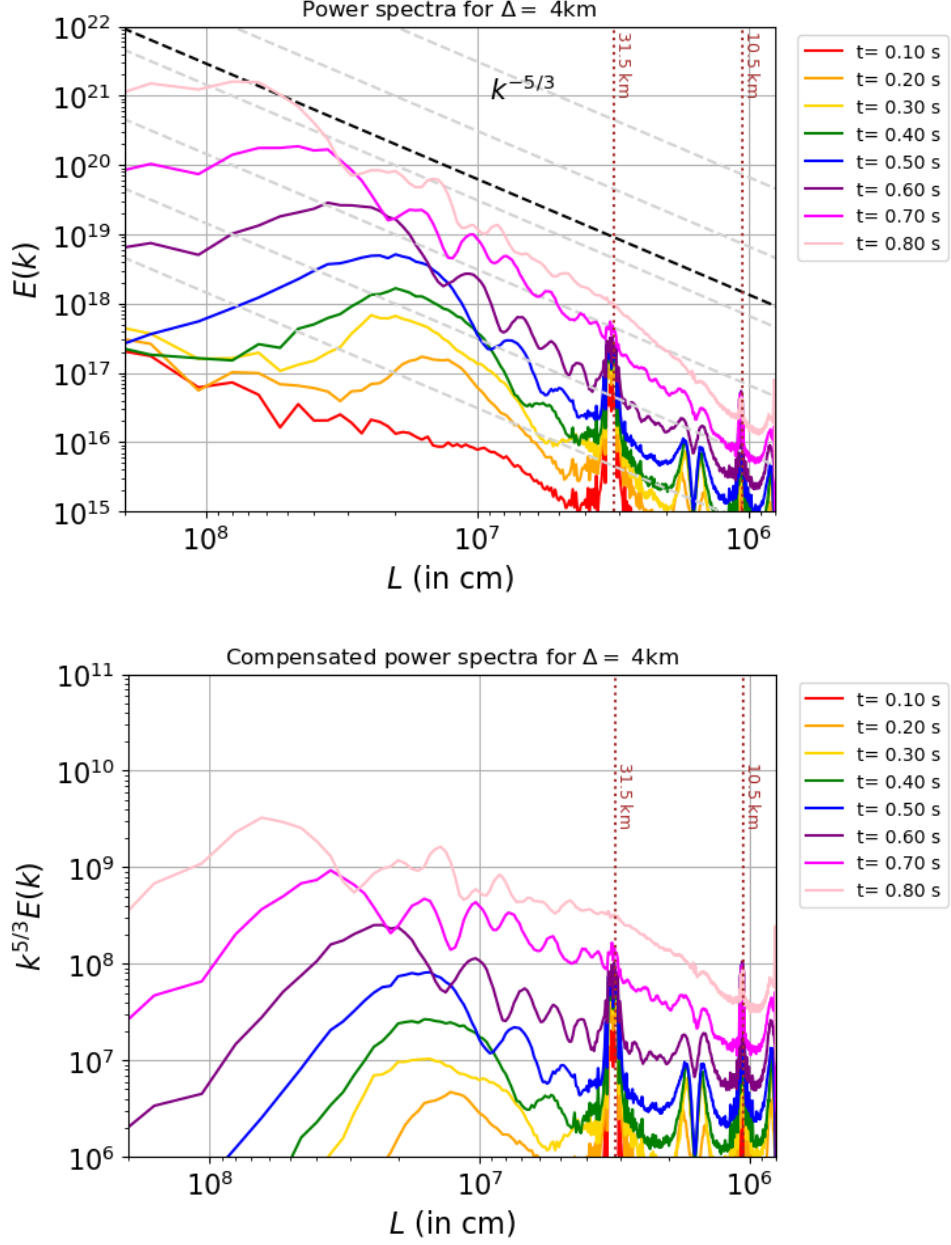


Figure 3.3: The uncompensated and compensated ( $E(k) k^{5/3}$ ) turbulent energy spectra for a standard density ( $\rho_c = 2.2 \times 10^9 \text{ g/cm}^3$ ) near- $M_{\text{Ch}}$  white dwarf ignited 50 km from the center, at  $t = 0.1 - 0.8$  s post-ignition. The *dot-dashed* line represents the numerical dissipative range from 10.5 – 31.5 km, while x-axis ranges from the Nyquist lengthscale at 8 kilometers to 1600 kilometers (from right to left). The excised region used for the calculation was kept constant at  $L = 1600 \text{ km}$ .

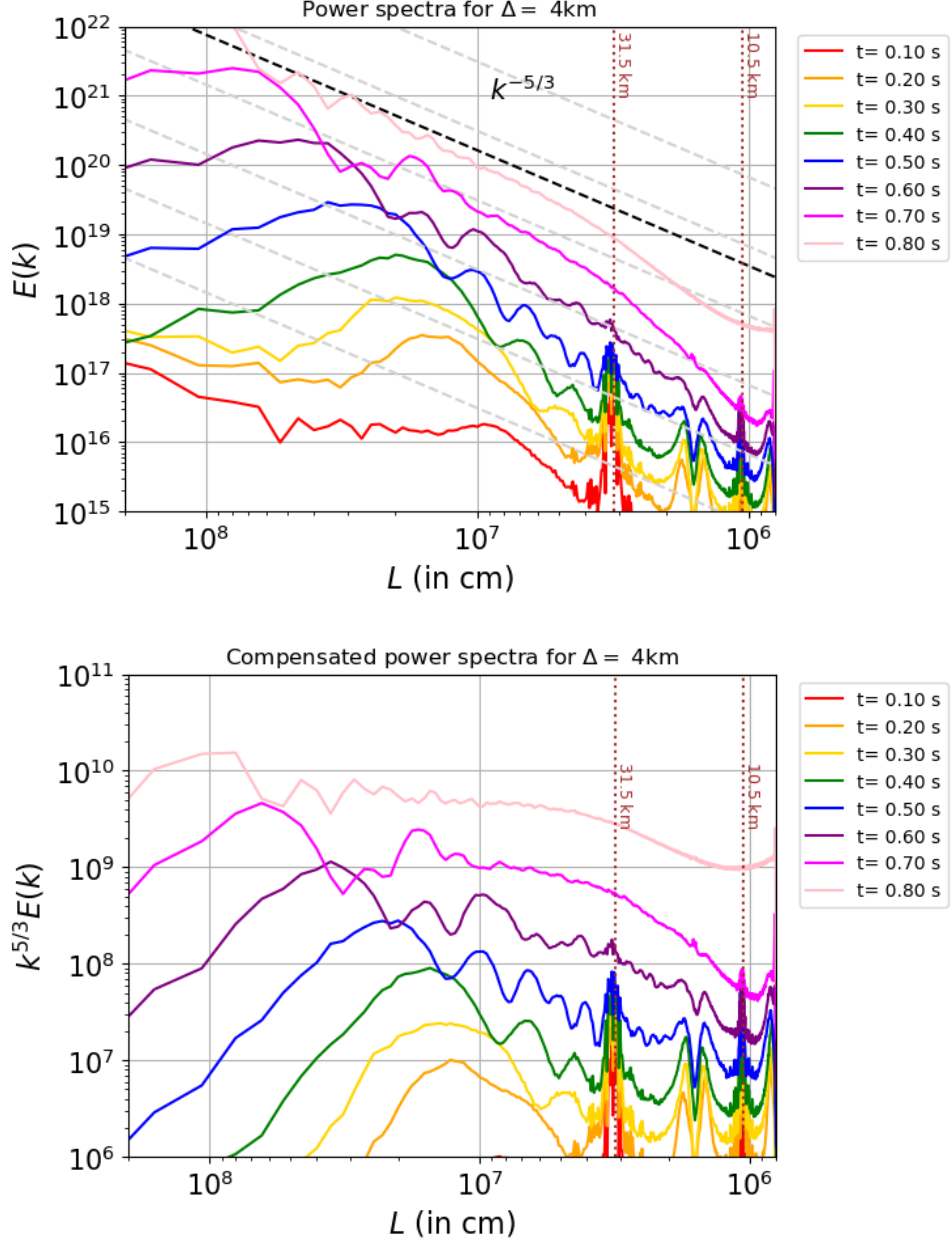


Figure 3.4: The uncompensated and compensated ( $E(k) k^{5/3}$ ) turbulent energy spectra for a standard density ( $\rho_c = 2.2 \times 10^9 \text{ g/cm}^3$ ) near- $M_{\text{Ch}}$  white dwarf ignited 100 km from the center, at  $t = 0.1 - 0.8$  s post-ignition. The *dot-dashed* line represents the numerical dissipative range from 10.5 – 31.5 km, while x-axis ranges from the Nyquist lengthscale at 8 kilometers to 1600 kilometers (from right to left). The excised region used for the calculation was kept constant at  $L = 1600$  km.

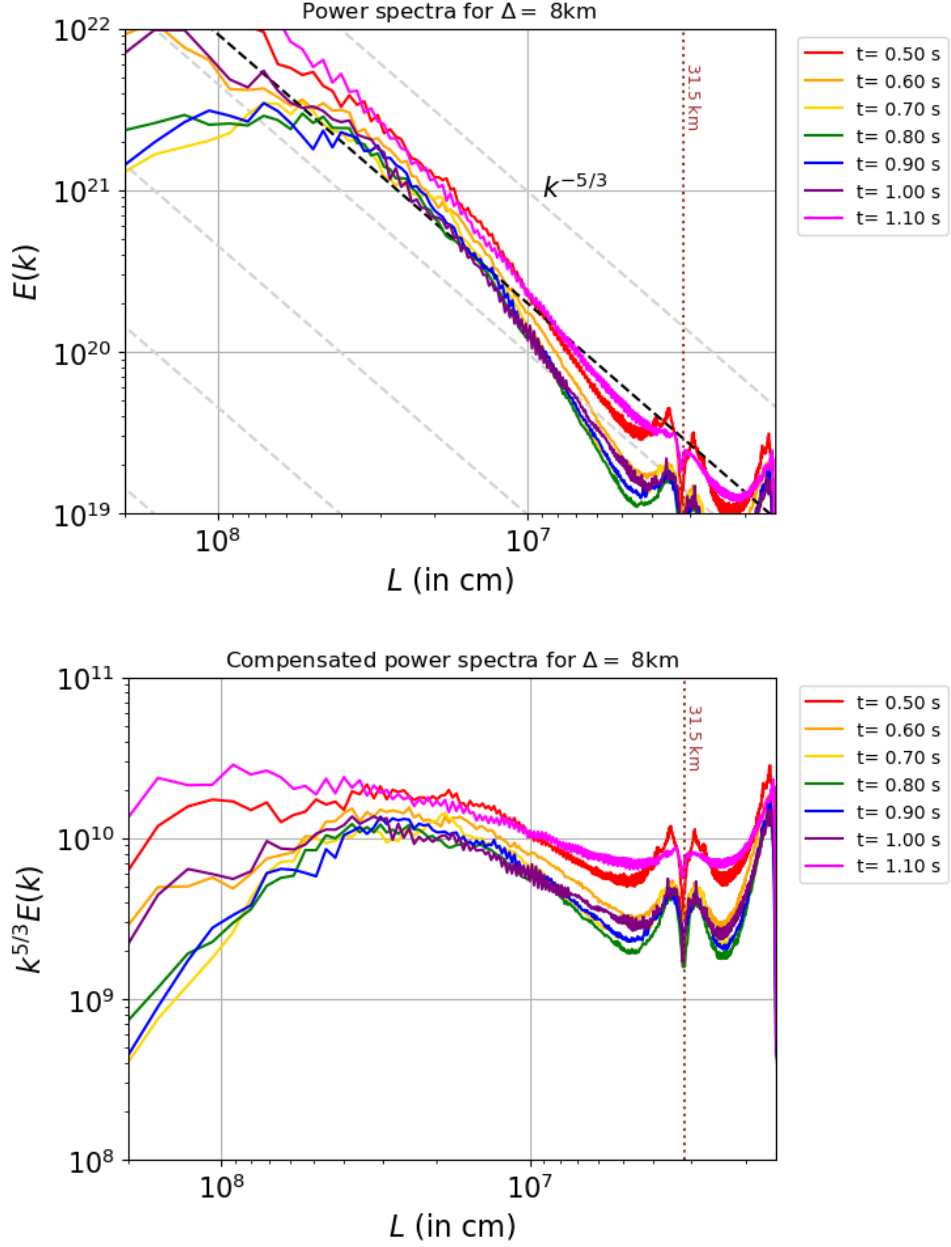


Figure 3.5: The un-compensated and compensated turbulent energy spectra ( $E(k)$   $k^{5/3}$ ) for a high density ( $\rho_c = 6.0 \times 10^9\text{ g/cm}^3$ ) near- $M_{\text{Ch}}$  white dwarf ignited 50 km from the center, at  $t = 0.5 - 1.1\text{ s}$  post-ignition. The excised region used for the calculation was kept constant at  $L = 3200\text{ km}$  for a maximum resolution of  $\Delta = 8\text{ km}$ .

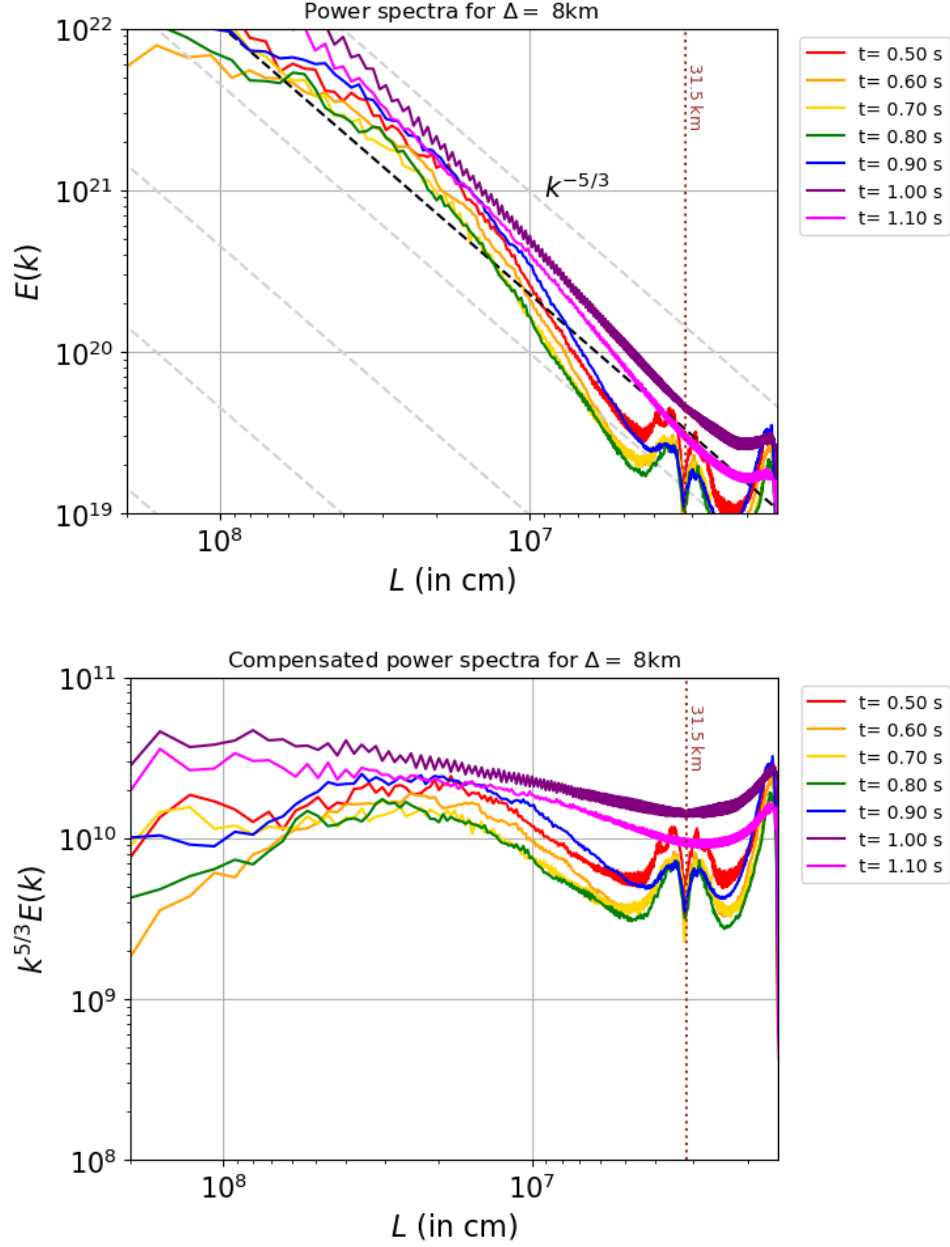


Figure 3.6: The un-compensated and compensated turbulent energy spectra ( $E(k)$   $k^{5/3}$ ) for a high density ( $\rho_c = 6.0 \times 10^9 \text{ g/cm}^3$ ) near- $M_{\text{Ch}}$  white dwarf ignited 100 km from the center, at  $t = 0.5 - 1.1$  s post-ignition. The excised region used for the calculation was kept constant at  $L = 3200 \text{ km}$  for a maximum resolution of  $\Delta = 8 \text{ km}$ .

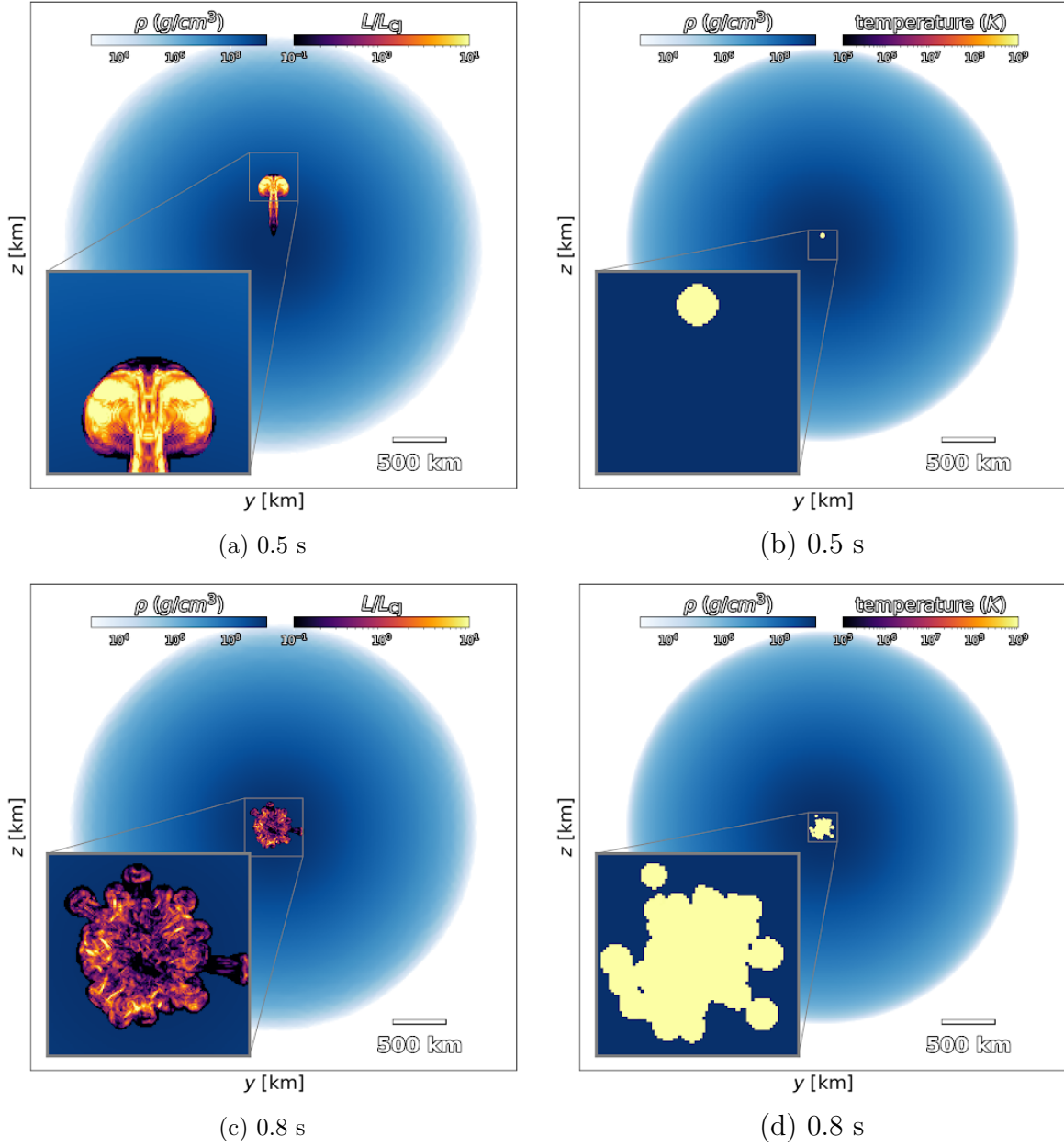


Figure 3.7: Overlay slice plots showing density (in blue), temperature (b and d), and the dimensionless ratio  $L/L_{CJ}$  (a and c) at the onset of tDDT driven detonation for  $N = 1$  and  $N = 100$  ignition models.

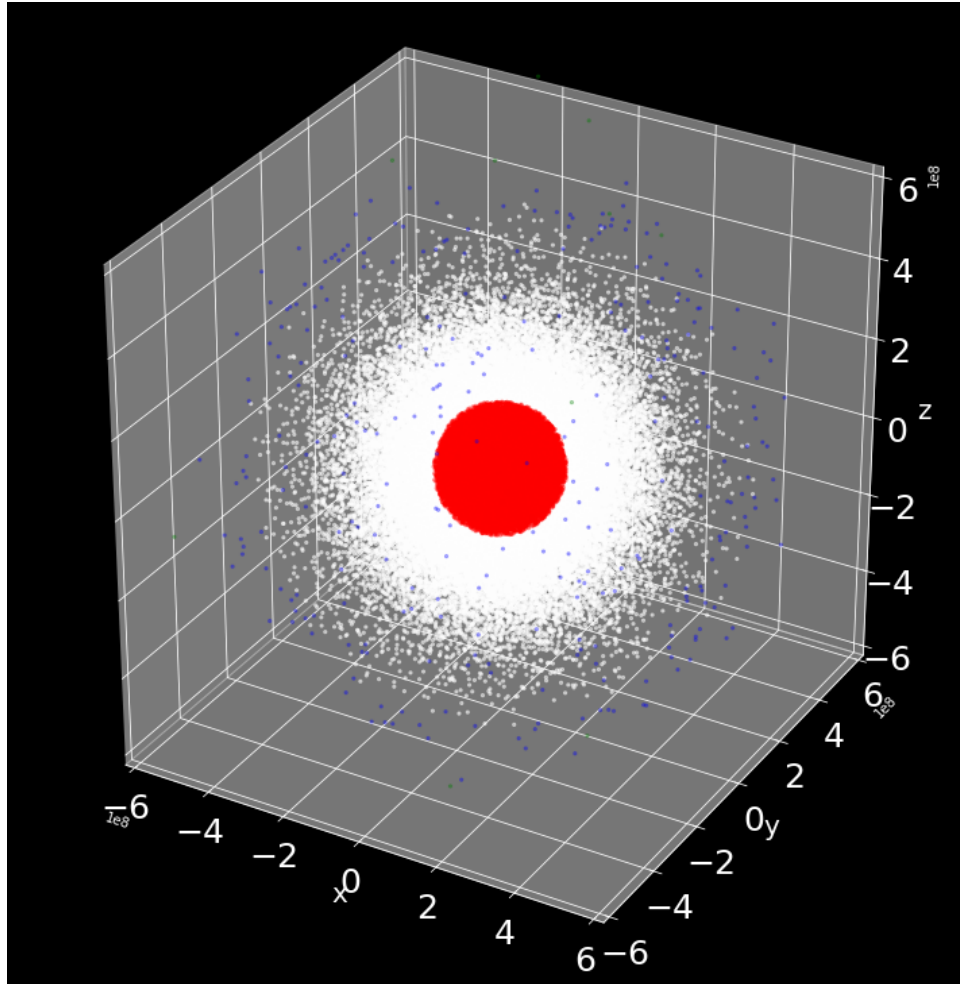


Figure 3.8: 3D scatter plot showing the distribution of nucleosynthetic yields, with colors marked to denote the kind of isotope with highest mass fraction per particle in a  $N = 10^5$  particle sample. Particles marked red represent high abundances of iron group elements ( $A > 40$ ,  $A \neq 56$  or  $Z \neq 28$ ). Particles marked white represent high abundances of radioactive isotope Ni-56. Particles marked blue represent intermediate mass elements ( $16 < A \leq 40$ ). This snapshot was taken at nuclear freeze-out.



Table 3.1: Nucleosynthetic yields (stable and radioactive) in excess of  $10^{-6}$  solar masses calculated from the  $N = 100$  standard density model using a 489-isotope network in Torch (Timmes, 1999a). The top three yield abundances are displayed in **boldface**.

Mass (in $M_{\odot}$ )	Isotope	Mass (in $M_{\odot}$ )	Isotope	Mass (in $M_{\odot}$ )	Isotope	Mass (in $M_{\odot}$ )	Isotope
0.0161	He-4	3.71e-05	V-47	<b>0.105</b>	<b>Fe-54</b>	0.00237	Cu-59
0.00012	O-16	1.58e-05	V-48	0.00851	Fe-55	0.0003	Cu-60
1.05e-05	Mg-24	3.47e-05	V-49	0.00536	Fe-56	0.000223	Cu-61
0.00226	Si-28	5.47e-06	V-50	0.000199	Fe-57	1.67e-05	Cu-62
1.21e-06	P-31	1.07e-05	V-51	2.75e-05	Fe-58	7.55e-06	Cu-63
5.95e-06	S-30	0.0003	Cr-48	1.43e-06	Co-53	0.000255	Zn-59
0.00163	S-32	0.000314	Cr-49	0.000227	Co-54	0.00664	Zn-60
2.27e-06	S-33	0.00266	Cr-50	0.0828	Co-55	0.000244	Zn-61
1.38e-06	S-34	0.000324	Cr-51	0.0117	Co-56	0.000655	Zn-62
4e-06	Cl-35	0.000657	Cr-52	0.00758	Co-57	1.04e-05	Zn-63
3.35e-06	Ar-34	3.2e-05	Cr-53	0.000327	Co-58	7.63e-06	Zn-64
0.000509	Ar-36	5.83e-06	Cr-54	9.33e-05	Co-59	6.68e-06	Ga-62
2.68e-06	Ar-37	1.11e-05	Mn-50	2.51e-06	Co-60	1.21e-05	Ga-63
3.46e-06	Ar-38	0.00215	Mn-51	1.77e-05	Ci-55	3e-05	Ge-63
1.14e-05	K-39	0.00104	Mn-52	<b>0.882</b>	<b>Ni-56</b>	0.000187	Ge-64
0.000724	Ca-40	0.0034	Mn-53	0.0861	Ni-57	1.05e-06	Ge-65
4.27e-06	Ca-41	0.000259	Mn-54	<b>0.122</b>	<b>Ni-58</b>	8.97e-06	Ge-66
1.63e-06	Ca-42	0.000102	Mn-55	0.00428	Ni-59	2.15e-06	Se-68
2.05e-05	Ti-44	1.58e-06	Mn-56	0.00159	Ni-60		
5.54e-06	Ti-45	3.43e-06	Fe-50	8.23e-05	Ni-61		
3.81e-05	Ti-46	2.13e-06	Fe-51	2.42e-05	Ni-62		
3.81e-06	Ti-47	0.00771	Fe-52	6.32e-06	Cu-57		
5.24e-06	Ti-48	0.0082	Fe-53	0.000495	Cu-58		

## Chapter 4 Conclusions and possible extensions

In this thesis, we applied *for the first time* a laboratory-validated turbulently-driven deflagration-to-detonation (tDDT) mechanism to full star 3D simulations of near-MCh white dwarfs. To determine when to apply the tDDT criterion, we analyze the turbulence in the flame by performing Fourier analysis on the kinetic energy at different scales, and determine when the turbulence becomes Kolmogorov. We found that the flame is eventually driven by Kolmogorov turbulence from an initially Rayleigh-Taylor driven propagation at late times and prior to bubble breakout. The time at which this transition happens coincide with the usual period when the DDT is triggered using a transition density of  $\sim 10^7$  g/cm<sup>3</sup>, near the white dwarf surface. If we assume Kolmogorov turbulence conditions at time  $t = 0$ , detonation onset conditions occurs promptly and with a higher transition density,  $\rho_c = 2.62 \times 10^8$  g/cm<sup>3</sup> for single bubble, and  $\rho_c = 1.76 \times 10^9$  g/cm<sup>3</sup> for multiple bubble ignition. Prompt detonations could yield higher Ni-56 abundances which lead to bright normal or overluminous 91T-like events. We found that for the  $N = 100$  model, the Ni-56 yield is  $\sim 0.8 M_\odot$  which is higher than literature values at  $0.6 M_\odot$  (Byrohl et al., 2019).

This work, however, is limited to a limited sample of models with varying ignition offsets, central densities, and maximum resolution. In the future, we wish to consider different initial conditions for near-Chandrasekhar mass white dwarfs, while carefully considering the central offset. Fisher & Jumper (2015) studied the dependence of the critical bubble offset on central density between scenarios where the bubble burns through the center of the white dwarf or is buoyantly driven. It is also important to note that despite observing an inertial range in the turbulence energy spectra we obtained, the inertial range may be limited by numerical dissipation. Pushing the simulations to higher resolutions could better resolve the physical inertial range that might be buried beneath the numerical dissipation range at early times. After developing the pipeline for offline turbulence statistics analysis, we will produce tDDT

initiated detonation models, obtain nucleosynthetic yields, calculate synthetic spectra, and cross-match with templates of observed events. We are also looking into developing modules to perform zoom-in simulations in regions where tDDT is highly probable using adaptive mesh refinement and embedded direct numerical simulations.

## References

- Abbott, T. M. C., Allam, S., Andersen, P., et al. 2019, *Astrophys. J. Lett.*, 872, L30
- Arnett, D., & Livne, E. 1994a, *Astrophys. J.*, 427, 315
- . 1994b, *Astrophys. J.*, 427, 330
- Bauer, E. B., Chandra, V., Shen, K. J., & Hermes, J. 2021, *Astrophys. J. Lett.*, 923, L34
- Bloom, J. S., Kasen, D., Shen, K. J., et al. 2011, *Astrophys. J. Lett.*, 744, L17
- Boos, S. J., Townsley, D. M., Shen, K. J., Caldwell, S., & Miles, B. J. 2021, *Astrophys. J.*, 919, 126
- Brooker, E., Plewa, T., & Fenn, D. 2021, *Mon. Not. R. Astron. Soc. Lett.*, 501, L23
- Byrohl, C., Fisher, R., & Townsley, D. 2019, *Astrophys. J.*, 878, 67, doi: 10.3847/1538-4357/ab1f73
- Colin, O., Ducros, F., Veynante, D., & Poinso, T. 2000, *Phys. Fluids*, 12, 1843, doi: 10.1063/1.870436
- Dan, M., Rosswog, S., Guillochon, J., & Ramirez-Ruiz, E. 2011, *Astrophys. J.*, 737, 89
- . 2012, *Mon. Not. R. Astron. Soc.*, 422, 2417
- Dilday, B., Howell, D., Cenko, S., et al. 2012, *Science*, 337, 942
- Dubey, A., Reid, L. B., Weide, K., et al. 2009, arXiv e-prints, arXiv:0903.4875. <https://arxiv.org/abs/0903.4875>
- Dubey, A., Antypas, K., Calder, A. C., et al. 2014, *The International Journal of High Performance Computing Applications*, 28, 225, doi: 10.1177/1094342013505656
- Fink, M., Röpke, F., Hillebrandt, W., et al. 2010, *Astron. Astrophys.*, 514, A53
- Fisher, R., & Jumper, K. 2015, *Astrophys. J.*, 805, 150, doi: 10.1088/0004-637X/805/2/150
- Foley, R., Bloom, J. S., Cenko, S. B., et al. 2019, *Bull. Am. Astron. Soc.*, 51, 305
- Fryxell, B., Olson, K., Ricker, P., et al. 2010, FLASH: Adaptive Mesh Hydrodynamics Code for Modeling Astrophysical Thermonuclear Flashes, Astrophysics Source Code Library, record ascl:1010.082. <http://ascl.net/1010.082>
- Gamezo, V. N., Khokhlov, A. M., & Oran, E. S. 2004, *Phys. Rev. Lett.*, 92, 211102
- Gilfanov, M., & Bogdán, Á. 2010, *Nature*, 463, 924

- Greggio, L., & Renzini, A. 1983, *Astron. Astrophys.*, 118, 217
- Han, Z., & Podsiadlowski, P. 2004, *Mon. Not. R. Astron. Soc.*, 350, 1301
- Hicken, M., Wood-Vasey, W. M., Blondin, S., et al. 2009, *Astrophys. J.*, 700, 1097
- Jackson, A. P., Calder, A. C., Townsley, D. M., et al. 2010, *Astrophys. J.*, 720, 99
- Kenworthy, W., Jones, D., Dai, M., et al. 2021, *Astrophys. J.*, 923, 265
- Khokhlov, A. 1991, *Astron. Astrophys.*, 245, 114
- Khokhlov, A., Mueller, E., & Höflich, P. 1993, *Astron. Astrophys.*, 270, 223
- Leibundgut, B., & Sullivan, M. 2018, *Space Sci. Rev.*, 214, 1
- Livne, E., Tuchman, Y., & Wheeler, J. 1991, in *Supernovae* (Springer), 219–222
- Ma, H., Woosley, S., Malone, C., Almgren, A., & Bell, J. 2013, *Astrophys. J.*, 771, 58
- Magee, M., Maguire, K., Kotak, R., & Sim, S. 2021, *Mon. Not. R. Astron. Soc.*, 502, 3533
- Mao, Y.-Y., Peter, A. H. G., Adhikari, S., et al. 2022, arXiv e-prints
- Mochkovitch, R., & Livio, M. 1990, *Astron. Astrophys.*, 236, 378
- Nomoto, K., & Leung, S.-C. 2018, *Space Sci. Rev.*, 214, 1
- Olling, R. P., Mushotzky, R., Shaya, E. J., et al. 2015, *Nature*, 521, 332
- Pakmor, R., Kromer, M., Röpke, F. K., et al. 2010, *Nature*, 463, 61
- Pakmor, R., Zenati, Y., Perets, H. B., & Toonen, S. 2021, *Mon. Not. R. Astron. Soc.*, 503, 4734
- Papish, O., & Perets, H. B. 2016, *Astrophys. J.*, 822, 19
- Pérez-Torres, M., Lundqvist, P., Beswick, R., et al. 2014, *Astrophys. J.*, 792, 38
- Pinsonneault, M., & Stanek, K. 2006, *Astrophys. J. Lett.*, 639, L67
- Poludnenko, A. Y., Chambers, J., Ahmed, K., Gamezo, V. N., & Taylor, B. D. 2019, *Science*, 366, eaau7365
- Poludnenko, A. Y., Gardiner, T. A., & Oran, E. S. 2011, *Phys. Rev. Lett.*, 107, 054501
- Sand, D., Sarbadhicary, S., Pellegrino, C., et al. 2021, *Astrophys. J.*, 922, 21
- Schaefer, B. E., & Pagnotta, A. 2012, *Nature*, 481, 164
- Scolnic, D. M., Jones, D. O., Rest, A., et al. 2018, *Astrophys. J.*, 859, 101

- Seitenzahl, I. R., Ciaraldi-Schoolmann, F., Röpke, F. K., et al. 2013, *Mon. Not. R. Astron. Soc.*, 429, 1156, doi: 10.1093/mnras/sts402
- Shen, K. J. 2015, *Astrophys. J. Lett.*, 805, L6
- Shen, K. J., Boubert, D., Gänsicke, B. T., et al. 2018, *Astrophys. J.*, 865, 15
- Tanikawa, A., Nomoto, K., Nakasato, N., & Maeda, K. 2019, *Astrophys. J.*, 885, 103
- Timmes, F. 1999a, *Astrophys. J. Suppl. Ser.*, 124, 241
- Timmes, F. X. 1999b, *Astrophys. J., Suppl. Ser.*, 124, 241–263, doi: 10.1086/313257
- Timmes, F. X., Brown, E. F., & Truran, J. 2003, *Astrophys. J.*, 590, L83
- Townsley, D. M., Calder, A. C., Asida, S. M., et al. 2007, *Astrophys. J.*, 668, 1118, doi: 10.1086/521013
- Townsley, D. M., Jackson, A. P., Calder, A. C., et al. 2009, *Astrophys. J.*, 701, 1582, doi: 10.1088/0004-637X/701/2/1582
- Tucker, M., Shappee, B., Vallely, P., et al. 2020, *Mon. Not. R. Astron. Soc.*, 493, 1044
- Van Kerkwijk, M. H., Chang, P., & Justham, S. 2010, *Astrophys. J. Lett.*, 722, L157
- Whelan, J., & Iben Jr, I. 1973, *Astrophys. J.*, 186, 1007
- Yamaoka, H., Nomoto, K., Shigeyama, T., & Thielemann, F.-K. 1992, *Astrophys. J.*, 393, L55
- Zingale, M., Almgren, A. S., Bell, J. B., Nonaka, A., & Woosley, S. E. 2009, *Astrophys. J.*, 704, 196
- Zingale, M., Woosley, S., Rendleman, C., Day, M., & Bell, J. 2005, *Astrophys. J.*, 632, 1021